Computational modeling of porous shape memory alloys

M. Panico [a], L.C. Brinson [a,b,*]

[a] Department of Mechanical Engineering, Northwestern University, 2145 Sheridan Road, Evanston, IL 60208-3111, USA
[b] Department of Materials Science and Engineering, Northwestern University, 2145 Sheridan Road, Evanston, IL 60208-3111, USA

ABSTRACT

In this study the mesoscopic behavior of porous shape memory alloys has been simulated with particular attention to the mechanical response under cyclic loading conditions. A recently developed constitutive law, accounting for full martensite reorientation as well as phase transformation, was implemented into the commercial finite element code ABAQUS. Due to stress concentrations in a porous microstructure, the constitutive law was enhanced to account for the development of permanent inelasticity in the shape memory matrix. With this simulation method, the complex interaction between porosity, local phase transformation and macroscale response has been evaluated. The results have implications for use of porous SMAs in biomedical and structural applications.

© 2008 Elsevier Ltd. All rights reserved.

1. Introduction

In the last two decades shape memory alloys (SMA) have found a large number of potential applications in several industrial fields ranging from aerospace to medical device industries. Recently, porous shape memory alloys have attracted great interest as low-weight materials with high energy dissipation properties (Zhao et al., 2005, 2006). In the biomedical field, owing to their biocompatibility and their promise to exhibit high strength and low modulus, NiTi foams have been tested as bone implant materials, successfully exhibiting a significant amount of bone ingrowth (Ayers et al., 1999; Simske and Sachdeva, 1995). NiTi foams, compared to the other biocompatible metallic foams, allow the elastic modulus of bone to be matched at smaller values of porosity (Greiner et al., 2005), resulting in increased fatigue life of the porous implant. Additionally, open porosity, when present, allows the bone tissue to grow into the implant improving its attachment and assimilation performance (Li et al., 2004; Shen et al., 2006; Spoerke et al., 2005, 2008). Moreover, when properly designed, phase transformation in the porous NiTi microstructure allows a larger macroscopic strain to be applied on the foam without significant permanent deformation via the pseudoelastic effect.

From the structural point of view, non-SMA metallic foams are currently being used for the fabrication of shock absorbing devices due to their superior energy dissipation capabilities compared to the corresponding dense materials (Degischer and Kriszt, 2002). Energy dissipation is enhanced by the presence of pores which increase the specific absorption capacity by scattering the impact shock waves. In a similar manner SMA foams are envisioned to provide an even larger damping capacity due to the dissipation deriving from the phase transformation in the SMA matrix in addition to the one resulting from the material porosity.

Several experimental techniques have been adopted to produce NiTi foams. Porous NiTi was first obtained by sintering of elemental Ni and Ti powders without pressure application (Li et al., 1998a,b) or by self-propagating high-temperature synthesis, SHS (Li et al., 2000). However, both these processes resulted in an incomplete reaction with presence of undesirable

---

* Corresponding author. Tel.: +1 847 467 2347; fax: +1 847 463 0540.
E-mail address: cbrinson@northwestern.edu (L.C. Brinson).

intermetallic phases (Ni$_3$Ti and Ti$_2$Ni) which makes the foams brittle and mildly superelastic. Recently, a technique based on hot-isostatic pressing (HIP) of mixed elemental Ni and Ti powders in the presence of Ar gas was proposed (Lagoudas and Vandygriff, 2002). These foams had a porosity of approximately 50% and were able to recover up to 3.5% strain even though the unwanted phases were not completely eliminated. Oppenheimer et al. (2004) have achieved better results in terms of composition and recoverable strain by using pre-alloyed NiTi powder producing foams with a porosity up to 25%. NiTi foams with a porosity of approximately 40% exhibiting shape memory effect have also been obtained by HIP of a mixture of NiTi and NaF powders and subsequently dissolving the NaF phase (Bansiddhi and Dunand, 2007). This last technique is the only one to allow for independent control of volume fraction and pore size by changing the amount and the characteristics of the NaF powder. However, the internal surfaces of the pores are irregular and rough due to the shape of the salt crystals and sintering of NiTi powder.

From the modeling point of view, metallic cellular materials have been extensively investigated (Gibson and Ashby, 1999). However, this kind of modeling approach was based on beam theory and can only be applied to high porosity foams. Recently, several authors (Entchev and Lagoudas, 2002, 2004; Nemat-Nasser et al., 2005; Qidwai et al., 2001) have used micromechanical averaging techniques in order to investigate the mechanical response of porous SMAs. In these analyses, the porous material is treated as a composite with SMA as the matrix and pores as the inclusions. Both the Mori-Tanaka and the self-consistent method have been used as averaging schemes for the prediction of the macroscopic response of the heterogeneous porous material, but in both cases the interaction among pores can only be accounted for in an approximate way.

A different approach that has been adopted to study the behavior of porous materials is based on the assumption of having a periodic distribution of pores. In this case symmetry arguments reduce the problem to the numerical analysis of a single unit cell on which appropriate boundary conditions need to be applied (Achenbach and Zhu, 1990; Nemat-Nasser and Hori, 1999; Qidwai et al., 2001). This method gives useful limiting predictions on the material macroscopic response and the way it is affected by pore volume fraction and pore shape. However, the assumption of a regular distribution of pores deviates significantly from the irregularity of real microstructures and will overestimate material response.

Extending the numerical unit cell approach, several authors (Benke and Weichert, 2003; DeGiorgi and Qidwai, 2002; Li et al., 2004; Segurado and Llorca, 2002; Shen and Brinson, 2007; Shen et al., 2006; Sihn and Roy, 2004; Thelen et al., 2004) have investigated the mechanical behavior of porous materials by simulating an opportunely defined representative volume element with many interconnected pores. Both 2D and 3D simulations have been adopted and the limitations of using simplified 2D models have been identified (Shen and Brinson, 2007). While most of the RVE methods for porous metals have been applied to non-SMA materials, DeGiorgi and Qidwai (2002) have used a simplified 2D model to describe the mesoscopic behavior of porous SMAs. Although they were able to capture the dependence of the transformation characteristics on porosity, their approach is limited in the fact that they only consider two-dimensional simulation cells and their constitutive model does not account for permanent inelasticity or reorientation effects.

In this paper, following this line of work, we perform 3D mesoscale simulations of SMA foams in order to investigate their material behavior with particular emphasis on the material response under cycling loading conditions and the accumulation of "irreversible martensite", i.e. martensite that cannot be converted back into austenite upon unloading. This is achieved by utilizing a recent developed SMA constitutive law (Panico and Brinson, 2007) based on the classical framework of thermodynamics of irreversible processes which robustly predicts the effect of multiaxial stress states and non-proportional loading histories. Moreover, the model is able to account for the evolution of both twinned and detwinned martensite and the reorientation process of the product phase according to loading direction. In order to apply this constitutive model to the study of porous SMAs, it was implemented into ABAQUS by developing a user material subroutine. The paper is organized as follows. In Section 2 we briefly introduce the constitutive model that we have used for the SMA matrix. We then describe the implementation of this constitutive law into ABAQUS and present the RVE model of a porous SMA. Section 3 illustrates the main results of our numerical simulations on the RVE SMA model, while Section 4 draws conclusions of our study.

2. Computational setup

2.1. SMA constitutive model

The SMA constitutive model used in this study has been developed and tested in a previous article (Panico and Brinson, 2007). Here, we will only discuss the main characteristics of this model, its implementation into finite elements, and a new feature that allows description of the SMA mechanical behavior under cyclic loading conditions. Further details about the constitutive law formulation can be found in the aforementioned reference.

Several experimental works (Liu et al., 1999; Malecot et al., 2006; Strnadel et al., 1995) have highlighted that shape memory alloys may develop irreversible strains during a cyclic loading process which appear to reach a saturation condition after a certain number of cycles. This has been attributed to the development of plastic strains and microstructural defects that inhibit complete reverse transformation of martensite. Therefore, in a similar fashion to other models existing in literature (Auricchio et al., 2007; Lagoudas and Entchev, 2004; Malecot et al., 2006), we have extended our previous constitutive model to account for this type of permanent inelasticity by introducing an additional internal variable which describes the evolution of irreversible martensite in the material.

Our SMA constitutive model (Panico and Brinson, 2007) assumes small strains and is developed within the framework of thermodynamics of irreversible processes. The formulation was specifically intended to capture the effect of reorientation of martensite variants according to loading direction. Therefore, the total strain rate is decomposed in three contributions, respectively, deriving from elastic strain, transformation of parent phase and reorientation of previously existing martensite variants:

$$\dot{\underline{\varepsilon}} = \dot{\underline{\varepsilon}}^{e} + \dot{\underline{\varepsilon}}^{tr} + \dot{\underline{\varepsilon}}^{re}. \tag{1}$$

In order to determine the relevant evolution laws, we start from the Helmoltz free energy of the three phase system which can be written as

$$\psi(\underline{\varepsilon}^{e}, T, z_{\sigma}, z_{T}, h) = \psi_0(\underline{\varepsilon}^{e}, T, z_{\sigma}, z_{T}) + \psi_h(z_{\sigma}, z_{T}, h), \tag{2}$$

where $\underline{\varepsilon}^{e}$ and T are the control variables, elastic strain tensor and absolute temperature while z_{σ}, z_{T} and h are the internal variables, respectively volume fractions of detwinned martensite, twinned martensite[1] and irreversible martensite. Similar to Malecot et al. (2006), in this paper we modify the free energy with an additional contribution to account for the decrease of free energy due to the development of material permanent inelasticity. Specifically, the following expression is assumed:

$$\psi_h(z_{\sigma}, z_{T}, h) = \psi_h^{0} - z\Delta\Pi_0(h), \tag{3}$$

where ψ_h^{0} is a material constant, $z = z_{\sigma} + z_{T}$ is the total martensite volume fraction and $\Delta\Pi_0(h)$ is an increasing function of h:

$$\Delta\Pi_0(h) = \psi_1^{0}h + \frac{1}{2}\psi_2^{0}h^2 \tag{4}$$

with ψ_1^{0} and ψ_2^{0} material parameters. In order to derive the thermodynamic dissipative forces, we use the second law of thermodynamics which is written in the form of the Clausius–Duhem inequality as

$$\frac{1}{\rho}\underline{\sigma} : \dot{\underline{\varepsilon}} - \dot{\psi} - \eta\dot{T} - \frac{1}{\rho T}\underline{q} \cdot \operatorname{grad} T \geqslant 0 \tag{5}$$

with ρ material density, η system entropy and $\underline{q}$ heat flux vector. By introducing the expression (2) for the free energy and considering only the mechanical dissipation potential:

$$\rho D_p = \rho\left(-\frac{\partial\psi}{\partial T} - \eta\right)\dot{T} + \left(\underline{\sigma} - \rho\frac{\partial\psi}{\partial\underline{\varepsilon}^{e}}\right) : \dot{\underline{\varepsilon}}^{e} + \underline{\sigma}' : \dot{\underline{\varepsilon}}^{tr} + \underline{\sigma}' : \dot{\underline{\varepsilon}}^{re} - \rho\frac{\partial\psi}{\partial z_{\sigma}}\dot{z}_{\sigma} - \rho\frac{\partial\psi}{\partial z_{T}}\dot{z}_{T} - \rho\frac{\partial\psi}{\partial h}\dot{h} \geqslant 0, \tag{6}$$

where $\underline{\sigma}'$ is the deviatoric part of the stress tensor; this leads to the two state equations

$$\eta = -\frac{\partial\psi}{\partial T} \quad \text{and} \quad \underline{\sigma} = \rho\frac{\partial\psi}{\partial\underline{\varepsilon}^{e}} = \underline{\underline{L}} : \underline{\varepsilon}^{e} \tag{7}$$

with $\underline{\underline{L}}$ being the elasticity tensor. Then, taking into account the relationship between $\dot{z}_{\sigma}$ and $\dot{\underline{\varepsilon}}^{tr}$ (Panico and Brinson, 2007), with some manipulations, Eq. (6) can be rewritten as

$$\rho D_p = \underline{X}_{tr} : \dot{\underline{\varepsilon}}^{tr} + \underline{X}_{re} : \dot{\underline{\varepsilon}}^{re} + X_{T}\dot{z}_{T} + X_h\dot{h} \geqslant 0, \tag{8}$$

where the X_α ($\alpha = tr, re, T, h$) are the thermodynamic forces conjugate to the internal variables. The expressions of these forces and more details on their analytical derivation can be found in Appendix A. At this point the following evolution laws for the internal variables are assumed:

$$\begin{aligned}
\dot{\underline{\varepsilon}}^{tr} &= \dot{\lambda}_{tr}\underline{X}_{tr}, \\
\dot{\underline{\varepsilon}}^{re} &= \dot{\lambda}_{re}\underline{\underline{\widehat{I}}} : \underline{X}_{re}, \\
\dot{z}_{T} &= \dot{\lambda}_{T}X_{T},
\end{aligned} \tag{9}$$

where the $\dot{\lambda}_\alpha$ ($\alpha = tr, re, T$) are positive Lagrange multipliers and the fourth-order tensor $\underline{\underline{\widehat{I}}}$ is the projection tensor of the total inelastic strain ensuring that the reorientation strain rate be zero for proportional loading histories. Regarding the internal variable h we have assumed the same evolution law as Malecot et al. (2006):

$$\dot{h} = m_0(h_\infty - h)^p\langle\dot{z}_{\sigma}\rangle. \tag{10}$$

In (10) $\langle\bullet\rangle$ indicates the positive part of its argument while m_0 and p are material parameters which determine how fast the asymptotic irreversible volume fraction value h_∞ is approached. The evolution law (10) was originally chosen in order to reproduce the experimental observations according to which irreversible strain increases only during forward

---

[1] Self-accommodated, or "twinned", martensite is formed by simple cooling under no external loading constraints. Then, typically 24 variants of equal volume fractions form in a self-accommodated fashion without significant macroscopic strain. In contrast, oriented, or "detwinned", martensite is produced by an applied stress and, consequently, the martensitic variants are preferentially oriented by the direction of the external force producing a macroscopic transformation strain.

transformation and tends to converge to an asymptotic limit value. With this choice of evolution kinetics it is easy to show that the Clausius–Duhem inequality is always satisfied since Eq. (8) can be written as

$$\dot{\lambda}_{tr}\underline{X}_{tr} : \underline{X}_{tr} + \dot{\lambda}_{re}\underline{X}_{re} : \widehat{\underline{\underline{I}}} : \underline{X}_{re} + \dot{\lambda}_T X_T X_T + X_h \dot{h} \geqslant 0. \tag{11}$$

The first and the third term are clearly non-negative while the second term is non-negative due to the nature of the tensor $\widehat{\underline{\underline{I}}}$ that is positive semi-definite. Finally, the fourth term is also non-negative since X_h is always greater or equal to zero with an appropriate choice of the parameters ψ_1^0 and ψ_2^0 while $\dot{h}$ is non-negative because of the assumed kinetics (10).

Table 1 summarizes the material parameters that have been adopted in this study, which capture a typical uniaxial response of shape memory materials. For instance in Fig. 1, we have illustrated the uniaxial mechanical response of a dense SMA simulated by our model with this set of parameters. The sample is subjected to cyclic loading conditions under stress control with a maximum applied value of 600 MPa for a total number of 15 loading cycles. We can notice a decrease in the onset of forward and reverse transformation (see Fig. 1a), which is in agreement with experimental observations and is a direct consequence of the energy decrease expressed by Eq. (3). Fig. 1b displays the increase in residual strain with the loading cycles due to the development of irreversible martensite. As a result of the evolution Eq. (10), the rate of increase of irreversible martensite is large in the first cycles and decreases in later cycles. The volume fraction of irreversible martensite asymptotically approaches h_∞, which means that the residual strain converges to $h_\infty \cdot \gamma$, which is equal to 1% in this situation (see Fig. 1b).

2.2. Finite element implementation

The SMA constitutive model has been implemented into a user subroutine for the commercial code ABAQUS. Particularly, we have chosen to adopt the explicit version of this finite element code to reduce the computational cost of our

Table 1
Material parameters adopted in the numerical simulations

Parameter	Value	Unit
E	38,000	MPa
v	0.36	–
γ	0.025	–
Δu_0	12,900	J/kg
$\Delta \eta_0$	47.5	J/kg K
H_σ	100	J/kg
ρ	8000	kg/m^3
A^f	10	MPa
B^f	30	MPa
C^f	60	MPa
A^r	10	MPa
B^r	30	MPa
C^r	150	MPa
Y_{re}	400	MPa^2
m_0	1.0	–
p	1.4	–
h_∞	0.4	–
ψ_1^0	400	J/kg
ψ_2^0	−1000	J/kg
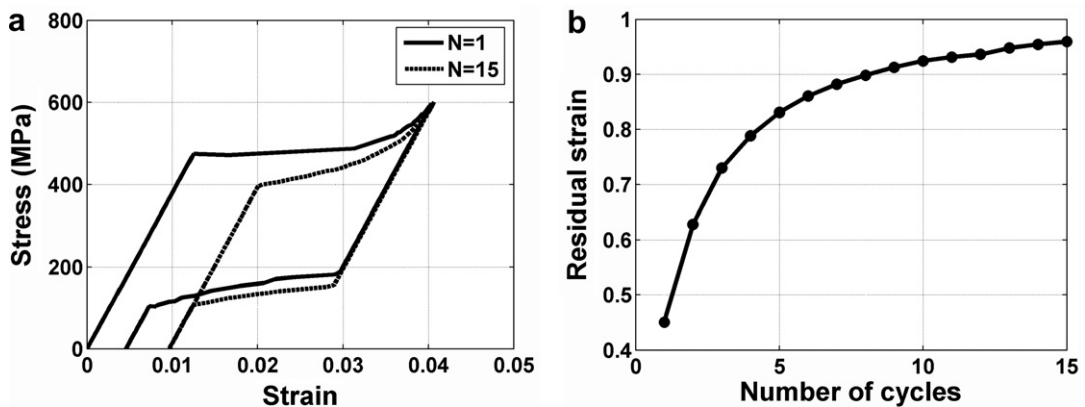
Fig. 1. Simulated constitutive response of a dense SMA: (a) stress–strain curves for loading cycle 1 and 15; (b) plot of accumulated residual strain as a function of loading cycle.

simulations. In order to implement the constitutive model into finite element, a stress update algorithm is needed. The numerical algorithm that we have adopted is similar to the return mapping schemes typical of plasticity theories. In order to define the material elastic regime, two limit functions have been defined respectively corresponding to transformation of parent phase ($F_{tr} = \|\underline{X}_{tr}\| - Y_{tr}$) and reorientation of martensite variants ($F_{re} = \frac{1}{2}\underline{X}_{re} : \underline{\widehat{I}} : \underline{X}_{re} - Y_{re}$) where Y_{tr} is a function of z_σ governing the transformation kinetics, and Y_{re} is a material parameter that determine the onset of the reorientation process.

Now, we describe the procedure that updates the internal variables and the stress tensor ($\underline{\varepsilon}^{in}_{n+1}, z_{\sigma_{n+1}}, z_{T_{n+1}}, h_{n+1}, \underline{\sigma}_{n+1}$) given the current strain and the values of the internal variables at the previous step ($\underline{\varepsilon}_{n+1}, \underline{\varepsilon}^{in}_n, z_{\sigma_n}, z_{T_n}, h_n$). For simplicity, in this section all the quantities without a subscript are intended to be values computed at time step $n + 1$. First an elastic trial stress is computed by assuming that the material behaves elastically during the time step ($\underline{\sigma}^{trial} = \underline{L} : (\underline{\varepsilon} - \underline{\varepsilon}^{in}_n)$). Then, based on this elastic prediction the two limit functions are computed. If the limit functions are both negative then the material response is elastic and the trial stress ($\underline{\sigma}^{trial}$) is taken as the updated stress. If any of the two limit functions has a positive value then an inelastic correction for the material response needs to be computed. This is accomplished by using a Newton–Raphson iteration scheme. For brevity, we will only detail this method for the case in which both the limit functions are positive (simultaneous transformation and reorientation). The other two situations (pure transformation: $F_{tr} > 0$ and $F_{re} < 0$; pure reorientation: $F_{tr} < 0$ and $F_{re} > 0$) can be easily obtained from the more general case by reducing the number of governing equations. The residual equations are the following:

$$\{a\} = \begin{Bmatrix} \underline{X}_{tr} - \underline{\sigma}' + \rho\left[\langle T\Delta\eta_0 - \Delta u_0\rangle + H_\sigma z_\sigma - \left(\psi^0_1 h_n + \frac{1}{2}\psi^0_2 h^2_n\right)\right]\frac{\underline{\varepsilon}^{in}}{\sqrt{3/2\gamma}\|\underline{\varepsilon}^{in}\|} \\ \underline{X}_{re} - \underline{\sigma}' \\ z_\sigma - \frac{\|\underline{\varepsilon}^{in}\|}{\sqrt{3/2\gamma}} \\ \|\underline{X}_{tr}\| - Y_{tr} \\ \frac{1}{2}\underline{X}_{re} : \underline{\widehat{I}} : \underline{X}_{re} - Y_{re} \\ \underline{\varepsilon}^{in} - \underline{\varepsilon}^{in}_n - \Delta\lambda_{tr}\underline{X}_{tr} - \Delta\lambda_{re}\underline{\widehat{I}} : \underline{X}_{re} \\ \underline{\sigma} - \underline{L} : (\underline{\varepsilon} - \underline{\varepsilon}^{in}) \end{Bmatrix} = \{0\} \tag{12}$$

with vector of unknowns $\{x\}=\{\underline{X}_{tr}, \underline{X}_{re}, z_\sigma, \Delta\lambda_{tr}, \Delta\lambda_{re}, \underline{\varepsilon}^{in}, \underline{\sigma}\}$. The solution vector $\{x^*\}$ may be found by means of a Newton iteration. Toward this purpose, the Jacobian matrix is computed:

$$[D] = \frac{\partial\{a\}}{\partial\{x\}} \tag{13}$$

and Eq. (12) are linearized as

$$[D] \cdot \{\Delta x\} + \{a\} = \{0\}. \tag{14}$$

Then, the increment of the unknowns vector can be computed as

$$\{\Delta x\} = -[D]^{-1} \cdot \{a\}. \tag{15}$$

This procedure can be iterated starting from the initial guess $\{x\} = \{\underline{X}_{tr_n}, \underline{X}_{re_n}, z_{\sigma_n}, \Delta\lambda_{tr_n}, \Delta\lambda_{re_n}, \underline{\varepsilon}^{in}_n, \underline{\sigma}^{trial}\}$ until Eq. (12) are satisfied within a certain tolerance. After convergence is attained the increment of internal variable h is explicitly computed

Table 2
Numerical algorithm for integration of SMA constitutive model

(1) Elastic stress predictor: $\underline{\sigma}^{trial} = \underline{L} : (\underline{\varepsilon} - \underline{\varepsilon}^{in}_n)$
(2) Check for transformation and/or reorientation: $F_\alpha(\underline{\sigma}^{trial}, T, \underline{\varepsilon}^{in}_n) \geqslant 0$, ($\alpha$ = tr,re)
(3) No. Elastic step: $\underline{\sigma} = \underline{\sigma}^{trial}$; $\underline{\varepsilon}^{in} = \underline{\varepsilon}^{in}_n$. Exit.
(4) Yes. Iterate for $\underline{X}_{tr}, \underline{X}_{re}, z_\sigma, \Delta\lambda_{tr}, \Delta\lambda_{re}, \underline{\varepsilon}^{in}, \underline{\sigma}$:
  If $\|a^{(k)}\| < TOL$, converged. Else:
  (a) Compute increments:
  $\{\Delta x^{(k)}\} = -[D^{(k)}]^{-1} \cdot \{a^{(k)}\}$
  (b) Update variables:
  $\{x^{k+1}\} = \{x^k\} + \{\Delta x^{(k)}\}$
  (c) $k \leftarrow k + 1$, go to 4
(5) Update h: $\Delta h_n = m_0(h_\infty - h_n)^p\langle\Delta z_{\sigma_n}\rangle$, $h_{n+1} = h_n + \Delta h_n$
(6) Check constraints: $h \leqslant z_\sigma \leqslant 1$
  (a) If $z_\sigma > 1 \Rightarrow \underline{\varepsilon}^{in} = \sqrt{3/2}\gamma \cdot (\underline{\varepsilon}^{in(k+1)}/\|\underline{\varepsilon}^{in(k+1)}\|)$
  (b) If $z_\sigma < h \Rightarrow \underline{\varepsilon}^{in} = h \cdot \sqrt{3/2}\gamma \cdot (\underline{\varepsilon}^{in(k+1)}/\|\underline{\varepsilon}^{in(k+1)}\|)$
7) Update z_T:
  (a) If $z_{\sigma_{n+1}} + z_{T_n} > 1 \Rightarrow \Delta z_{T_n} = -\Delta z_{\sigma_n}$
  (b) Else if $M^0_s < T < M^0_f \Rightarrow \Delta z_{T_n} = (\Delta\eta_0/c^f) \cdot \langle-\Delta T\rangle$
  (c) Else if $A_s < T < A_f \Rightarrow \Delta z_{T_n} = -(\Delta\eta_0/c^f) \cdot \langle\Delta T\rangle$
  (d) Else $\Delta z_{T_n} = 0$

from the evolution law (10). Finally, the increment of twinned martensite volume fraction z_T can be computed from the temperature change and the increment of z_σ following the procedure illustrated in Table 2, which also summarizes the complete stress update algorithm. More details on the evolution of the internal variable z_T can be found in Panico and Brinson (2007).

2.3. Finite element model

The representative volume element is constructed from a cube with sides of 1 mm. The boundary conditions that we have applied to the computational domain are schematically illustrated in Fig. 2. The lateral faces of the cube are constrained to remain planar and normal to one of the coordinate axes. This type of boundary condition is periodic from a mechanical point of view, but not from a microstructural one which means that pores are not mirrored through opposing faces. As shown by Shen and Brinson (2006), this boundary constraint allows selection of a smaller size for the representative volume element. The bottom face is fixed in the loading direction y while a uniform pressure is applied on the top surface that is restricted to remain planar and normal to the loading axis.

A regular mesh made of 8000 eight-node brick elements is adopted and the porous microstructure is simulated by randomly assigning to some of these elements elastic material properties with negligible stiffness ($E_{pores} \cong 10^{-9} E_{SMA}$), similar to what was done for two dimensional finite element models by DeGiorgi and Qidwai (2002). Five different porous samples have been generated with pore volume fractions respectively of 0.1, 0.15, 0.2, 0.3 and 0.4. Fig. 3 shows the samples with volume fractions of 0.1 and 0.4 with the porous microstructure represented by the white elements. We have investigated the convergence of the mesoscopic response of the porous material with mesh refinement. As an example, the sample with the highest porosity (40%) has been generated with a mesh of 8000 elements and a much finer mesh of 64,000 elements (see Fig. 4). The two 40% samples have been tested under compression with a maximum applied stress of 400 MPa. The mesoscopic response is calculated by volume averages of the stress and strain components in the loading direction over the whole domain. Fig. 4 shows that the two mesoscopic responses are barely distinguishable which validates the use of the coarser mesh for the purpose of our study.

3. Results

The porous samples have been tested in compression under cyclic loading conditions to a maximum stress of 600 MPA for a total of 15 loading cycles at a temperature of 293 K, where the material behavior is pseudoelastic. In the following we will
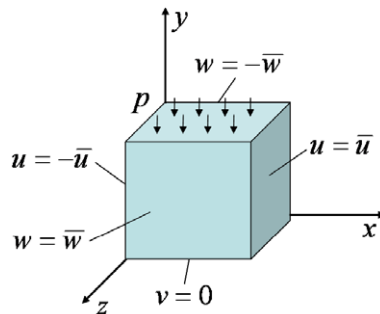

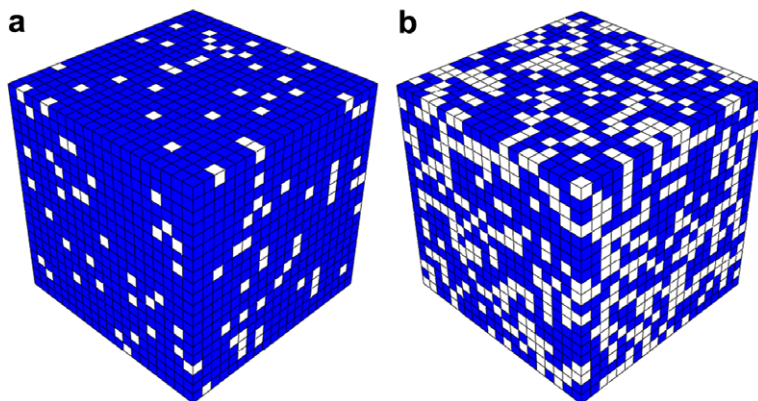Fig. 2. Schematic of computational domain and applied boundary conditions.

Fig. 3. Representative volume elements and finite element mesh for the samples with pore volume fraction of 0.1 and 0.4 with the porous microstructure represented by the white elements.
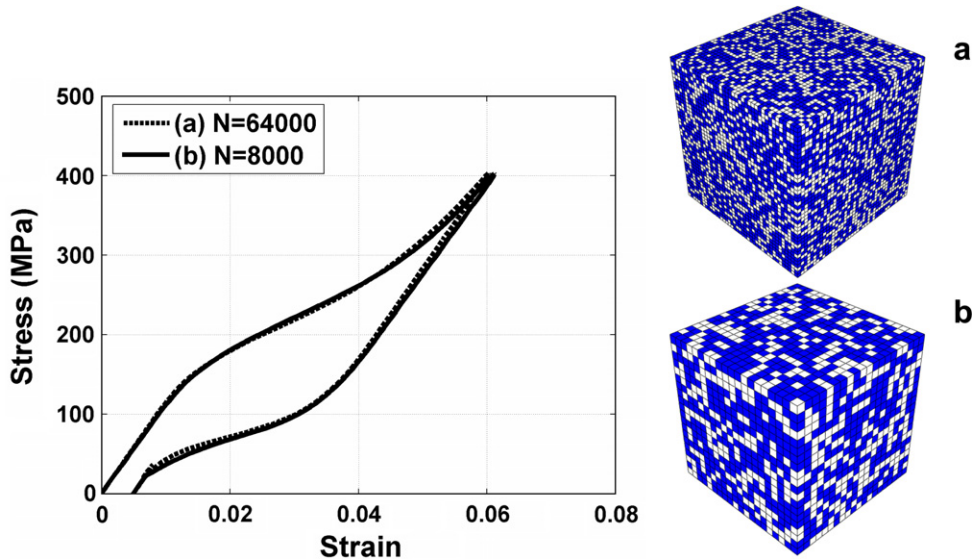
Fig. 4. Convergence study of the average stress strain response of the representative volume element, where *N* is the number of adopted finite elements.

illustrate the main results of our simulations: in Section 3.1 we will focus on the elastic properties of the porous samples; in Section 3.2 the transformation behavior of the porous material will be investigated; finally, Section 3.3 analyzes the material response to cyclic loading and the way this response is affected by the amount of porosity.

3.1. Simulation of elastic behavior

The effective elastic modulus for the porous material has been calculated from the mesoscopic stress–strain curve obtained from the finite element simulations and illustrated in Fig. 5a. The elastic modulus has been computed as the slope of the secant that connects the points at zero stress with the one at 10 MPa applied stress, in which region all the samples behave elastically. Fig. 5a shows the calculated values of elastic modulus for different pore volume fractions. As expected, this quantity rapidly decreases with porosity. In the same figure, we have also reported with a dashed line the result that would be obtained by applying the Gibson and Ashby formula ($E_{porous} = E_{bulk} (1 - f)^2$, with E_{bulk} = 38 GPa) (Gibson and Ashby, 1999). This formula was theoretically derived for the case of high porosity cellular materials but it can be empirically extended to lower porosities. It predicts that the elastic modulus decreases with the square of the porosity and shows a good qualitative agreement with our simulations up to porosities of 30%. This slight deviation from the theoretical prediction for the highest porosities is probably due to the increasing geometrical differences between our computational model and the assumption in the Gibson and Ashby formula of having a material which can be idealized through a structure of beams. Fig. 5b displays a plot of the stress concentration factor as a function of the material porosity. The concentration factor
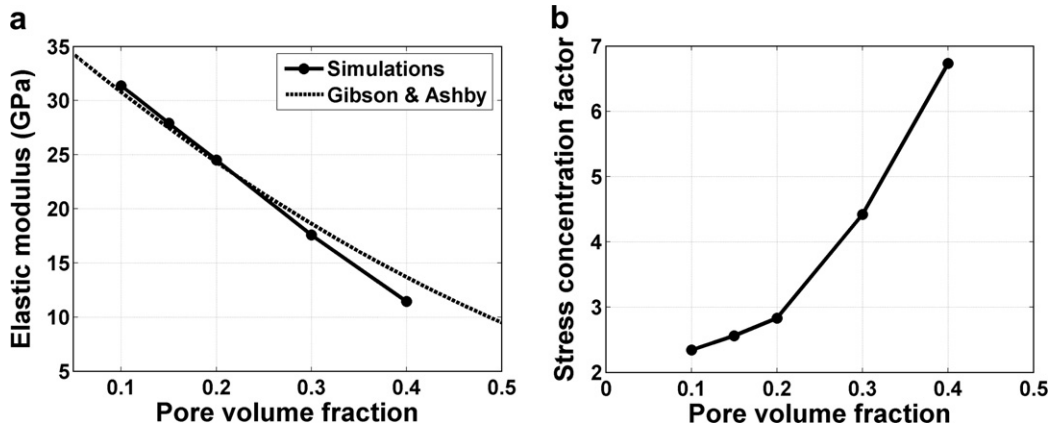

Fig. 5. Elastic properties of the porous samples: (a) effective elastic modulus versus pore volume fraction (the result of the simulations is compared with analytical predictions from the Gibson & Ashby formula); (b) stress concentration factor as a function of porosity.

has been calculated in the "elastic" regime (at an applied stress of approximately 60 MPa) as the ratio of the maximum longitudinal stress component in the representative volume element to the applied macroscopic stress. As expected, the stress concentration increases with porosity as a result of the larger pore interaction and inhomogeneity of the stress field. This is a very important characteristic in porous materials because high stress concentrations will produce a decrease of the material fatigue strength. Note that the stress concentration factor for a spherical hole is approximately 2, which explains the asymptotic limit towards which the stress intensity factor is converging at lower porosities. This elastic analysis demonstrates one of the advantages of porous SMAs. One main objective of bone implant applications is to match the elastic modulus of the implant material with the one of human bone (15–20 GPa) so that the so-called "stress shielding" effect is minimized. In the case of porous SMA and more specifically porous NiTi, this can be achieved at a relatively low porosity value at which stress concentration effects are still limited.

3.2. Pseudoelastic response

As previously mentioned, all the samples at different porosities have been subjected to a uniform pressure applied on the top surface of the representative volume element. Stress control conditions have been chosen rather than displacement control ones in order to compare the accumulated irreversible strain for the different material porosities under a common load. Moreover, a stress control condition best represents the typical loading for bone implant materials, one of the main proposed applications of SMA foams.

Fig. 6a shows the average stress–strain curve for the porous samples with volume fractions of 0.1, 0.2 and 0.4. In contrast to the sharply defined phase transformation for a fully dense SMA (as in Fig. 1a), a smooth transition between the initial elastic phase and the transformation stage of the material behavior is observed for porous SMA. This result is in agreement with experimental measurements (Bansiddhi and Dunand, 2007; Greiner et al., 2005) and is due to the inhomogeneity of the stress field which results in a non-uniform evolution of the phase transformation at increasing levels of applied stress. As a consequence of this feature, one cannot discern a single stress value at which transformation is initiated. Therefore, in a similar fashion to metal plasticity, we have defined a critical stress for onset of phase transformation as the stress corresponding to an inelastic strain of 0.2%. Fig. 6b displays a plot of the critical transformation stress as a function of the material porosity. As expected the value of the critical stress decreases with the pore volume fraction as a consequence of the larger stress concentrations. Another feature that may be noticed from Fig. 6a is that the hardening rate during phase transformation is much higher for the case of porous materials compared to the case of dense SMA. This result is again in agreement with experimental data and is due to the inhomogeneity of the stress field in porous samples which distributes the phase transformation over a larger range of applied macroscopic stress.

With the finite element simulations, we are able to investigate in more detail the evolution of martensite in the porous microstructure with increasing macroscopic applied stress. Toward this purpose we have subjected the samples to a larger maximum stress of 1200 MPa. Fig. 7a is a plot of the average detwinned martensite volume fraction in the SMA matrix as a function of the applied stress for the samples with porosities of 0.1, 0.2 and 0.4. From this plot, we notice that transformation starts macroscopically at a much lower stress for the sample with pore volume fraction of 0.4. However, the rate at which phase transformation evolves is smaller compared to the samples at lower porosities (0.1 and 0.2). Therefore, at a stress of approximately 600 MPa the situation is reversed and the low porosity samples present a larger value of the average martensite volume fraction. Fig. 7b and c shows the distribution of z_σ in the microstructure at the maximum applied stress of 1200 MPa, respectively, for material porosities of 0.1 and 0.4. It may be noticed that transformation cannot saturate the whole microstructure, i.e. there are regions which cannot reach a value of z_σ equal to 1 even for very high applied stress.
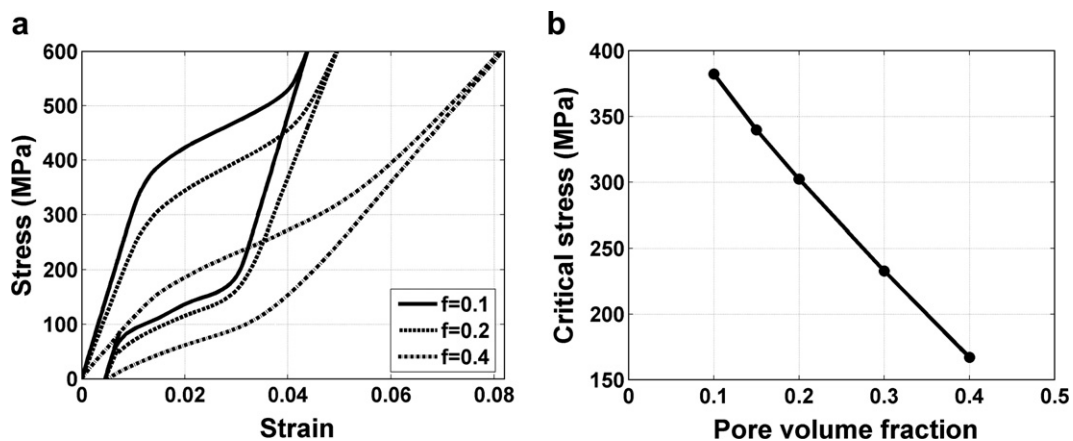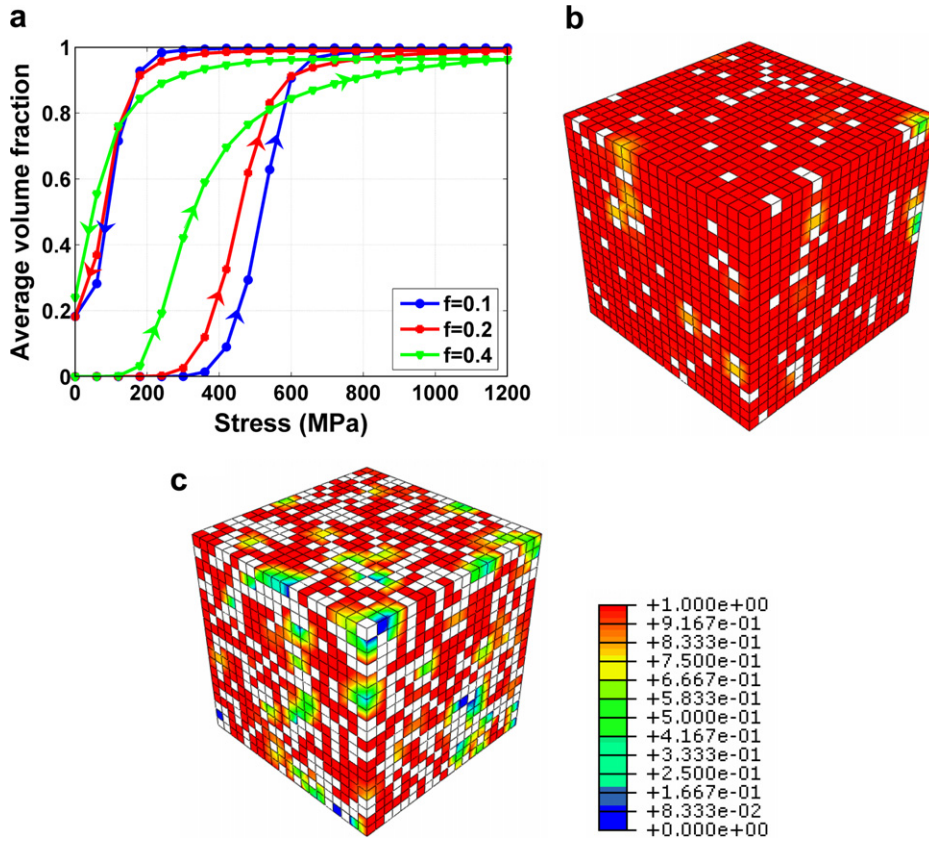

Fig. 6. Transformation behavior of the porous samples: (a) average stress–strain responses for the samples with pore volume fraction of 0.1, 0.2 and 0.4; (b) macroscopic critical stress for onset of transformation as a function of material porosity.

Fig. 7. Evolution of phase transformation and average detwinned martensite volume fraction in the porous samples: (a) average martensite volume fraction versus applied stress; (b) contour plot of martensite volume fraction at the maximum applied stress of 1200 MPa for the sample at 0.1 porosity; (c) contour plot of martensite volume fraction at the maximum applied stress of 1200 MPa for the sample at 0.4 porosity.

This is more evident for the case of 0.4 pore volume fraction. Thus, for increasing stress the average value of z_σ in the matrix approaches an asymptotic value lower than one (see Fig. 7a); moreover, this asymptotic value is smaller in the case of high porosity materials.

In order to analyze in more detail these results in Fig. 8a and b, we have plotted the probability density functions of the Mises equivalent stress for the samples with porosities of 0.1 and 0.4. The two figures corresponds to a macroscopic applied stress, respectively, of 360 and 720 MPa. In the same plots we have indicated with two dotted lines the stresses necessary to
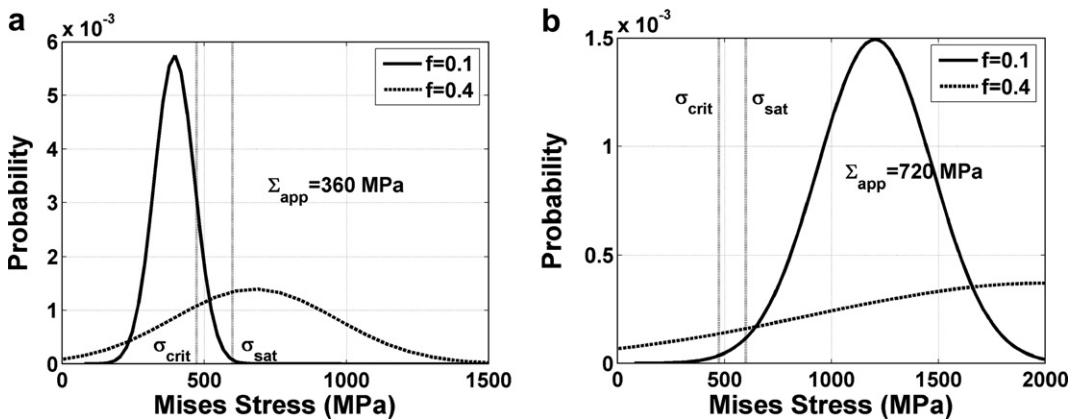
Fig. 8. Probability density functions of the Mises stress for the samples with porosities of 0.1 and 0.4: (a) applied stress of 360 MPa; (b) applied stress of 720 MPa.

initiate (σ_{crit}) and saturate (σ_{sat}) phase transformation in a non-porous sample. As expected high porosity results in a stress distribution with larger average value and greater standard deviation, while the stress distribution tends to be uniform in lower porosity cases. When the macroscopic applied stress is small (Fig. 8a), the material behavior is dominated by the average value of the stress which dictates the amount of material volume with a stress greater than the critical one σ_{crit}. Therefore, the sample with porosity 0.4 has a lower macroscopic activation stress and a larger amount of martensite at the low and intermediate levels of applied stress (see Fig. 7a).

On the other hand, for large values of applied stress, phase transformation is saturated in the highly stressed regions and the material transformation response is controlled by the areas at lower stress level. This feature can be observed in Fig. 8b, where the average values of the stress distributions have already overcome the stress required to complete transformation (σ_{sat}) for both porosity values. Therefore, in this condition of large macroscopic applied stress the broader stress distribution of high porosity sample will result in larger areas at a low stress level under the critical value (see Fig. 8b) and consequently a smaller total amount of phase transformation. The existence of these two different regimes for the porous transformation response explains the result in Fig. 7a, where at high stress levels low porosity samples exhibit a larger average martensite volume fraction than the high porosity one. Moreover, the fact that even for large applied macroscopic stresses there are significant regions of the sample with porosity 0.4, where the Mises stress does not reach the critical value makes it very difficult to saturate the transformation process in high porosity materials, as we had previously noticed from analysis of the results in Fig. 7a–c.

3.3. Cyclic loading behavior

In this section, we focus on the mechanical response of the porous samples to the cycling loading. In Fig. 9, we show the average stress–strain response to the 15 loading cycles for the sample with 0.2 pore volume fraction. In each cycle permanent strain accumulates, but the material response rapidly stabilizes towards an asymptotic transformation cycle. Fig. 10a–c shows the evolution of the volume fraction of irreversible martensite h for the sample with porosity 0.2 respectively at the end of loading cycles 1, 5 and 15. We notice that irreversible martensite accumulates in the material and at the end of the loading cycle 15 the asymptotic value h_∞ has been reached in most of the sample. Fig. 11 displays a plot of the residual macroscopic strain as a function of the loading cycles for the sample with pore volume fractions of 0.1, 0.2 and 0.4 and for the dense SMA material as well. For the same number of cycles the amount of residual strain is higher for larger porosities. This is particularly evident in the case of pore volume fractions larger than 0.2. It may also be noticed that for porous materials the residual macroscopic strain tends to an asymptotic value larger than in the case of the dense material (which is 1% using the parameters from Table 1). Moreover, the rate at which this asymptotic limit is approached is lower for porous samples.

In order to explain this result we can again consider the plots of Fig. 8 which show the distribution of the equivalent Mises stress in two porous samples. The higher the porosity of the material the more the stress is non-uniformly distributed in the microstructure. As a consequence a large number of loading cycles is needed to saturate the production process of irreversible martensite in the regions where stress concentrations are not present. Regarding the asymptotic limit value of the irreversible strain, it is clear that the presence of pores in the microstructure allows a larger macroscopic strain to be accommodated for the same value of average irreversible strain in the SMA matrix. Therefore, we can conclude that the porous nature of the microstructure enhances the phenomenon of accumulation of permanent inelasticity typical of the dense material. This is manifested in a higher asymptotic residual strain and in a slower convergence rate and is an important feature to consider in the design process of a porous SMA.
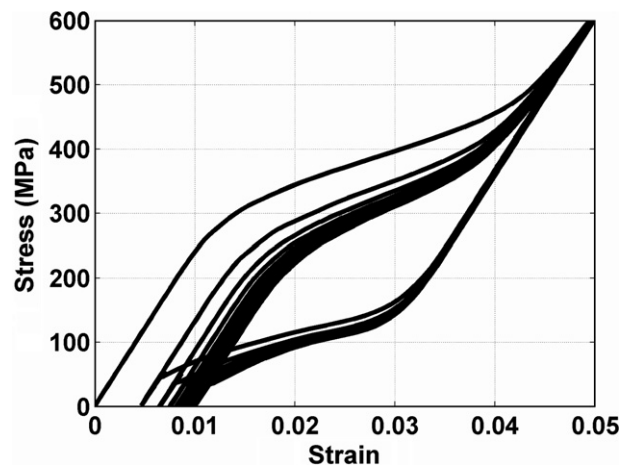

Fig. 9. Average stress–strain behavior under cyclic loading conditions for the sample with pore volume fraction of 0.2.
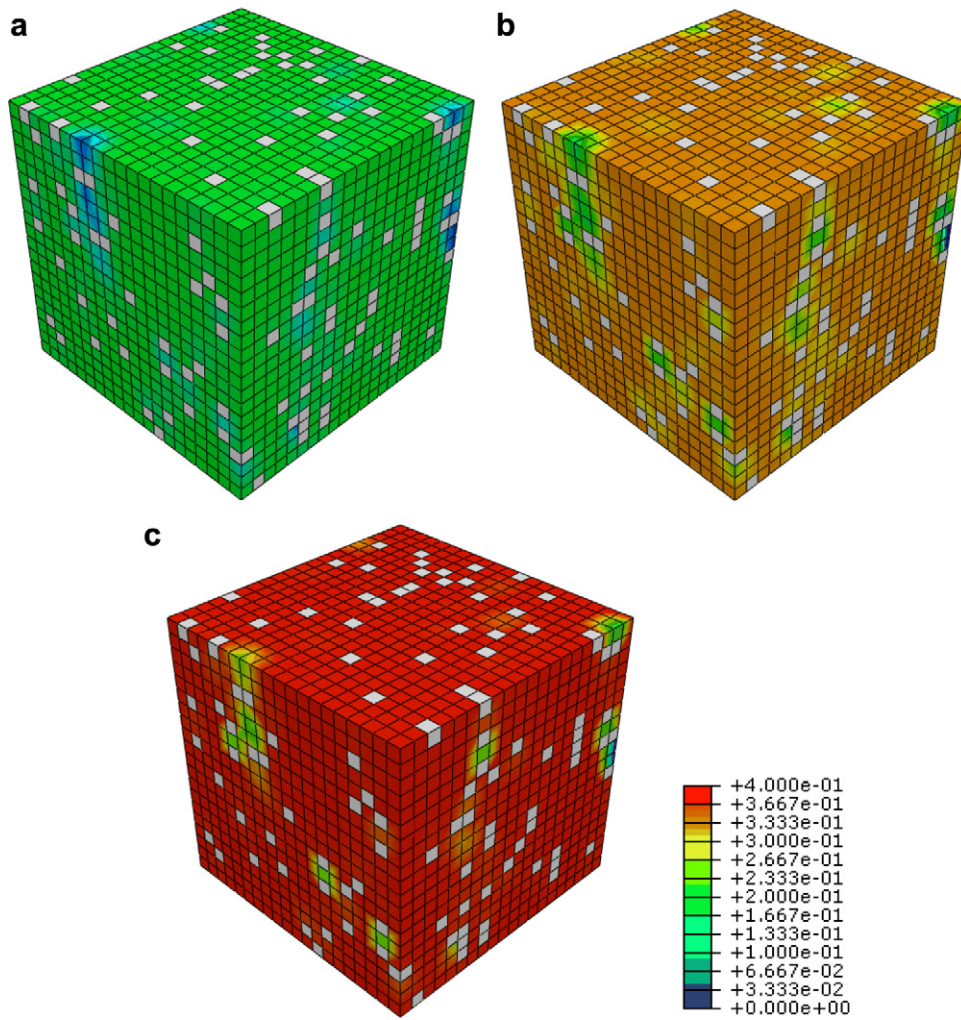
Fig. 10. Contour plots of the volume fraction of irreversible martensite at the end of loading cycle 1 (a), cycle 5 (b) and cycle 15 (c).
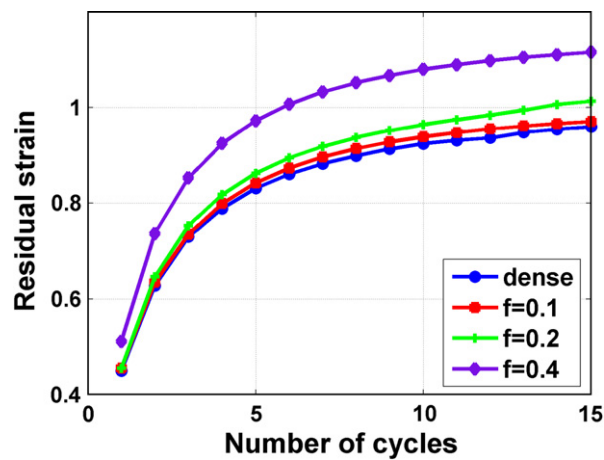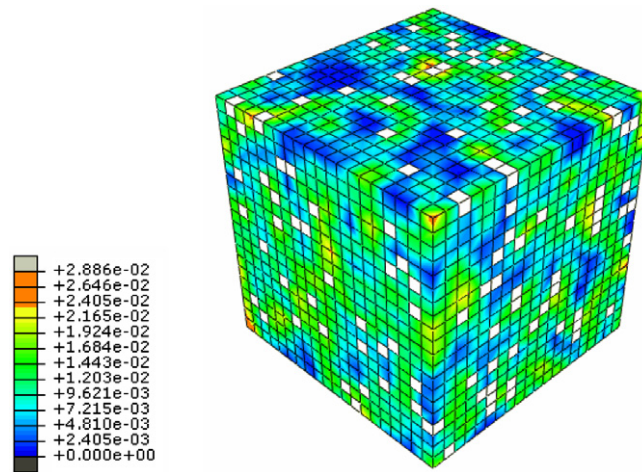

Fig. 11. Plot of the macroscopic residual strain accumulated in the porous sample as a function of the number of loading cycles for porosities of 0.1, 0.2, 0.4 and the dense SMA material.

Fig. 12. Contour plot of the norm of the cumulated reorientation strain for the sample with porosity 0.1 at the end of loading cycle 15. It is observed that reorientation strain is significant for porous materials even under macroscopically proportional loading cases.

3.4. Reorientation strain

Finally, in this section, we want to highlight the importance to properly account for the effect of martensite reorientation into our macroscopic phenomenological model. Therefore, we give the following definition of accumulated reorientation strain:

$$\underline{\varepsilon}^{re} = \int_0^t \underline{\dot{\varepsilon}}^{re} \, dt, \tag{16}$$

which is a measure of the amount of reorientation in a particular location at that moment in the simulation. In Fig. 12, we show a contour plot of the norm of the reorientation strain in Eq. (16) for the sample with porosity 0.1 at the end of the 15 loading cycles. We notice that this quantity has a non-negligible value in most of the sample volume. Thus, for the case of porous materials even when only a proportional macroscopic loading is applied it is still necessary to account for the strain contribution deriving from martensite reorientation. Indeed, the strong non-uniformity of the stress field and the scattering of elastic waves produced by the porous microstructure can locally result in a significant non-proportionality of the loading condition with the consequent production of reorientation strain.

4. Conclusions

In this work, we have investigated the mechanical response under cyclic loading conditions of porous SMA at different levels of pore volume fraction. Toward this purpose a criterion for accumulation of irreversible martensite was implemented in our recent SMA constitutive model (Panico and Brinson, 2007). This model was successfully implemented into finite element method and adopted to test porous representative volume elements under uniform pressure conditions. The effective elastic modulus of the porous samples was found to decrease with the pore volume fraction. At the same time, the stress concentration factor increases with porosity due to the enhanced pore interaction. We also found that the macroscopic stress necessary to initiate phase transformation is strongly affected by porosity due to the inhomogeneity of the stress field leading to highly stressed regions in the porous microstructure at relatively low level of the macroscopic applied loads. Moreover, we found that phase transformation cannot be saturated in the sample even for very large values of the applied stress and this feature is enhanced by the amount of porosity. We investigated the accumulation of permanent strains in the porous material with the subsequent loading cycles. It was found that permanent strains tend to a limit value which increases with material porosity. We have showed that for porous materials even for the case of macroscopic proportional loadings martensite reorientation may have a significant impact on the material response and needs to be properly accounted for.

Finally, we want to highlight that in this paper we have used a very simple idealized model based on cubic finite element cells in order to simulate the mesoscopic response of porous SMA. This approach is very efficient from a computational point of view, but in some cases may lack of accuracy and present clear limitations related to the idealized pore morphology. Modeling of more realistic porous SMA microstructures and comparing their response to the simplified models adopted here will be the subject of future work.

Acknowledgements

Appendix A

The Helmoltz free energy assumed in our SMA constitutive model has the following expression:

$$\psi(\underline{\varepsilon}^{e}, T, z_{\sigma}, z_{T}, h) = \frac{1}{2\rho}\underline{\varepsilon}^{e} : \underline{\underline{L}} : \underline{\varepsilon}^{e} + u_{o}^{A} - T\eta_{0}^{A} - z_{T}(\Delta u_{0} - T\Delta\eta_{0}) - z_{\sigma}\langle\Delta u_{0} - T\Delta\eta_{0}\rangle$$

$$+ c_{v}\left[(T - T_{0}) - T\ln\left(\frac{T}{T_{0}}\right)\right] + \frac{1}{2}H_{\sigma}z_{\sigma}^{2}\psi_{h}^{0} - z\left(\psi_{1}^{0}h + \frac{1}{2}\psi_{2}^{0}h^{2}\right), \tag{A.1}$$

where the following nomenclature is adopted: $\underline{\varepsilon}^{e}$, elastic strain tensor; T, absolute temperature; z_{σ}, volume fraction of detwinned martensite; z_{T}, volume fraction of twinned martensite; h, volume fraction of irreversible martensite; ρ, material density; u_{0}^{A}, austenite specific energy; η_{0}^{A}, austenite specific entropy; u_{0}^{M}, martensite specific energy; η_{0}^{M}, martensite specific entropy; $\Delta u_{0} = u_{0}^{A} - u_{0}^{M}$; $\Delta\eta_{0} = \eta_{0}^{A} - \eta_{0}^{M}$; c_{v}: specific heat at constant volume; T_{0}, equilibrium temperature; $z = z_{\sigma} + z_{T}$, total martensite volume fraction; $H_{\sigma}, \psi_{h}^{0}, \psi_{1}{}^{0}, \psi_{2}^{0}$, material parameters. The Clausius–Duhem inequality writes as, Eq. (6):

$$\rho D_{p} = \rho\left(-\frac{\partial\psi}{\partial T} - \eta\right)\dot{T} + (\underline{\sigma} - \rho\frac{\partial\psi}{\partial\underline{\varepsilon}^{e}}) : \underline{\dot{\varepsilon}}^{e} + \underline{\sigma}' : \underline{\dot{\varepsilon}}^{tr} + \underline{\sigma}' : \underline{\dot{\varepsilon}}^{re} - \rho\frac{\partial\psi}{\partial z_{\sigma}}\dot{z}_{\sigma} - \rho\frac{\partial\psi}{\partial z_{T}}\dot{z}_{T} - \rho\frac{\partial\psi}{\partial h}\dot{h} \geqslant 0. \tag{A.2}$$

However, from (Panico and Brinson, 2007)

$$\dot{z}_{\sigma} = \frac{\underline{\varepsilon}^{in} : \underline{\dot{\varepsilon}}^{tr}}{\sqrt{3/2}\gamma\|\underline{\varepsilon}^{in}\|}. \tag{A.3}$$

Then, introducing in Eq. (A.2):

$$\rho D_{p} = \rho\left(-\frac{\partial\psi}{\partial T} - \eta\right)\dot{T} + (\underline{\sigma} - \rho\frac{\partial\psi}{\partial\underline{\varepsilon}^{e}}) : \underline{\dot{\varepsilon}}^{e} + \left(\underline{\sigma}' - \rho\frac{\partial\psi}{\partial z_{\sigma}}\frac{\underline{\varepsilon}^{in}}{\sqrt{3/2}\gamma\|\underline{\varepsilon}^{in}\|}\right) : \underline{\dot{\varepsilon}}^{tr} + \underline{\sigma}' : \underline{\dot{\varepsilon}}^{re} - \rho\frac{\partial\psi}{\partial z_{T}}\dot{z}_{T} - \rho\frac{\partial\psi}{\partial h}\dot{h} \geqslant 0. \tag{A.4}$$

Thus, by adopting the expression (A.1) for the Helmoltz free energy and considering Eq. (8), we obtain

$$\eta = -\frac{\partial\psi}{\partial T} = c_{v}\ln\frac{T}{T_{0}} + \eta_{0}^{A} - z_{T}\Delta\eta_{0} - z_{\sigma}\Delta\eta_{0}\frac{\langle\Delta u_{0} - T\Delta\eta_{0}\rangle}{|\Delta u_{0} - T\Delta\eta_{0}|},$$

$$\underline{\sigma} = \rho\frac{\partial\psi}{\partial\underline{\varepsilon}^{e}} = \underline{\underline{L}} : \underline{\varepsilon}^{e},$$

$$\underline{X}_{tr} = \underline{\sigma}' - \rho\frac{\partial\psi}{\partial z_{\sigma}}\frac{\underline{\varepsilon}^{in}}{\sqrt{3/2}\gamma\|\underline{\varepsilon}^{in}\|}$$

$$= \underline{\sigma}' - \rho\left[\langle T\Delta\eta_{0} - \Delta u_{0}\rangle + H_{\sigma}z_{\sigma} - \left(\psi_{1}^{0}h + \frac{1}{2}\psi_{2}^{0}h^{2}\right)\right]\frac{\underline{\varepsilon}^{in}}{\sqrt{3/2}\gamma\|\underline{\varepsilon}^{in}\|}, \tag{A.5}$$

$$\underline{X}_{re} = \underline{\sigma}',$$

$$X_{T} = -\rho\frac{\partial\psi}{\partial z_{T}} = -\rho\left[(T\Delta\eta_{0} - \Delta u_{0}) - \left(\psi_{1}^{0}h + \frac{1}{2}\psi_{2}^{0}h^{2}\right)\right],$$

$$X_{h} = -\rho\frac{\partial\psi}{\partial h} = \rho z(\psi_{1}^{0} + \psi_{2}^{0}h).$$

References

Achenbach, J.D., Zhu, H., 1990. Effect of interphases on micro and macromechanical behavior of hexagonal-array fiber composites. Journal of Applied Mechanics – Transactions of the Asme 57 (4), 956–963.

Auricchio, F., Reali, A., Stefanelli, U., 2007. A three-dimensional model describing stress-induced solid phase transformation with permanent inelasticity. International Journal of Plasticity 23 (2), 207–226.

Ayers, R.A., Simske, S.J., Bateman, T.A., Petkus, A., Sachdeva, R.L.C., Gyunter, V.E., 1999. Effect of nitinol implant porosity on cranial bone ingrowth and apposition after 6 weeks. Journal of Biomedical Materials Research 45 (1), 42–47.

Bansiddhi, A., Dunand, D.C., 2007. Shape-memory NiTi foams produced by solid-state replication with NaF. Intermetallics 15 (12), 1612–1622.

Benke, S., Weichert, D., 2003. Meso-mechanical modeling of damage in metal foams. Advances in Fracture and Damage Mechanics, 345–349.

DeGiorgi, V.G., Qidwai, M.A., 2002. A computational mesoscale evaluation of material characteristics of porous shape memory alloys. Smart Materials & Structures 11 (3), 435–443.

Degischer, H.-P., Kriszt, B., 2002. Handbook of Cellular Metals: Production, Processing, Applications. Wiley, Weinheim.

Entchev, P.B., Lagoudas, D.C., 2002. Modeling porous shape memory alloys using micromechanical averaging techniques. Mechanics of Materials 34 (1), 1–24.

Entchev, P.B., Lagoudas, D.C., 2004. Modeling of transformation-induced plasticity and its effect on the behavior of porous shape memory alloys. Part II: porous SMA response. Mechanics of Materials 36 (9), 893–913.

Gibson, L.J., Ashby, M.F., 1999. Cellular Solids: Structure and Properties. Cambridge University Press, Cambridge.

Greiner, C., Oppenheimer, S.M., Dunand, D.C., 2005. High strength, low stiffness, porous NiTi with superelastic properties. Acta Biomaterialia 1 (6), 705–716.

Lagoudas, D.C., Entchev, P.B., 2004. Modeling of transformation-induced plasticity and its effect on the behavior of porous shape memory alloys. Part I: constitutive model for fully dense SMAs. Mechanics of Materials 36 (9), 865–892.

Lagoudas, D.C., Vandygriff, E.L., 2002. Processing and characterization of NiTi porous SMA by elevated pressure sintering. Journal of Intelligent Material Systems and Structures 13 (12), 837–850.

Li, B.Y., Rong, L.J., Li, Y.Y., 1998a. Porous NiTi alloy prepared from elemental powder sintering. Journal of Materials Research 13 (10), 2847–2851.

Li, B.Y., Rong, L.J., Li, Y.Y., 1998b. Anisotropy of dimensional change and its corresponding improvement by addition of TiH2 during elemental powder sintering of porous NiTi alloy. Materials Science and Engineering a-Structural Materials Properties Microstructure and Processing 255 (1-2), 70–74.

Li, B.Y., Rong, L.J., Li, Y.Y., Gjunter, V.E., 2000. Synthesis of porous Ni–Ti shape-memory alloys by self-propagating high-temperature synthesis: reaction mechanism and anisotropy in pore structure. Acta Materialia 48 (15), 3895–3904.

Li, H.L., Oppenheimer, S.M., Stupp, S.I., Dunand, D.C., Brinson, L.C., 2004. Effects of pore morphology and bone ingrowth on mechanical properties of microporous titanium as an orthopaedic implant material. Materials Transactions 45 (4), 1124–1131.

Liu, Y., Xie, Z.L., Van Humbeeck, J., 1999. Cyclic deformation of NiTi shape memory alloys. Materials Science and Engineering a – Structural Materials Properties Microstructure and Processing 275, 673–678.

Malecot, P., Lexcellent, C., Foltete, E., Collet, M., 2006. Shape memory alloys cyclic behavior: experimental study and modeling. Journal of Engineering Materials and Technology – Transactions of the Asme 128 (3), 335–345.

Nemat-Nasser, S., Hori, M., 1999. Micromechanics: overall properties of heterogeneous materials. Elsevier, Amsterdam; New York.

Nemat-Nasser, S., Su, Y., Guo, W.G., Isaacs, J., 2005. Experimental characterization and micromechanical modeling of superelastic response of a porous NiTi shape-memory alloy. Journal of the Mechanics and Physics of Solids 53 (10), 2320–2346.

Oppenheimer, S.M., O'Dwyer, J.G., Dunand, D.C., 2004. Porous superelastic NiTi produced by powder-metallurgy. TMS Letters 1 (5), 93–94.

Panico, M., Brinson, L.C., 2007. A three-dimensional phenomenological model for martensite reorientation in shape memory alloys. Journal of the Mechanics and Physics of Solids 55 (11), 2491–2511.

Qidwai, M.A., Entchev, P.B., Lagoudas, D.C., DeGiorgi, V.G., 2001. Modeling of the thermomechanical behavior of porous shape memory alloys. International Journal of Solids and Structures 38 (48-49), 8653–8671.

Segurado, J., Llorca, J., 2002. A numerical approximation to the elastic properties of sphere-reinforced composites. Journal of the Mechanics and Physics of Solids 50 (10), 2107–2121.

Shen, H., Brinson, L.C., 2006. A numerical investigation of the effect of boundary conditions and representative volume element size for porous titanium. Journal of Mechanics of Materials and Stuctures 1 (7), 1179–1204.

Shen, H., Brinson, L.C., 2007. Finite element modeling of porous titanium. International Journal of Solids and Structures 44 (1), 320–335.

Shen, H., Oppenheimer, S.M., Dunand, D.C., Brinson, L.C., 2006. Numerical modeling of pore size and distribution in foamed titanium. Mechanics of Materials 38 (8–10), 933–944.

Sihn, S.W., Roy, A.K., 2004. Modeling and prediction of bulk properties of open-cell carbon foam. Journal of the Mechanics and Physics of Solids 52 (1), 167–191.

Simske, S.J., Sachdeva, R., 1995. Cranial Bone Apposition and Ingrowth in a Porous Nickel-Titanium Implant. Journal of Biomedical Materials Research 29 (4), 527–533.

Spoerke, E.D., Murray, N.G., Li, H.L., Brinson, L.C., Dunand, D.C., Stupp, S.I., 2005. A bioactive titanium foam scaffold for bone repair. Acta Biomaterialia 1 (5), 523–533.

Spoerke, E.D., Murray, N.G., Li, H.L., Brinson, L.C., Dunand, D.C., Stupp, S.I., 2008. Titanium with aligned, elongated pores for orthopedic tissue engineering applications, pp. 402–412.

Strnadel, B., Ohashi, S., Ohtsuka, H., Miyazaki, S., 1995. Effect of mechanical cycling on the pseudoelasticity characteristics of Ti–Ni and Ti–Ni–Cu alloys. Materials Science and Engineering a – Structural Materials Properties Microstructure and Processing 203 (1-2), 187–196.

Thelen, S., Barthelat, F., Brinson, L.C., 2004. Mechanics considerations for microporous titanium as an orthopedic implant material. Journal of Biomedical Materials Research Part A 69A (4), 601–610.

Zhao, Y., Taya, M., Kang, Y.S., Kawasaki, A., 2005. Compression behavior of porous NiTi shape memory alloy. Acta Materialia 53 (2), 337–343.

Zhao, Y., Taya, M., Izui, H., 2006. Study on energy absorbing composite structure made of concentric NiTi spring and porous NiTi. International Journal of Solids and Structures 43 (9), 2497–2512.